Inner-valence photoionization of HCN: An example of the complete breakdown of the quasiparticle picture of photoionization

M. Wells and Robert R. Lucchese*
Department of Chemistry, Texas A&M University, College Station, Texas 77843-3255
(Received 3 May 1999)

We performed both single- and coupled-channel scattering calculations of the photoionization of HCN at a photon energy range of 40–1000 eV. Based upon the present results, we predict that HCN is a system for which the inner-valence photoionization is characterized by a complete breakdown of the quasiparticle picture of photoionization. We find that there is no inner valence main line and that the intensity from photoionization from the inner valence 3σ orbital is split into two prominent satellites and two weaker satellites. These four satellites occur at binding energies of approximately 27.0, 29.5, 31.0, and 33.0 eV, and are almost solely of inner valence origin. We identify these satellites as being of inner-valence origin as a consequence of the theoretically predicted high-energy convergence of the photoionization cross-section rations to the ratio of corresponding spectroscopic intensity factors. Additionally, we find that there is one mixed provenance satellite that occurs on the shoulder of the highest binding energy ($4\sigma^{-1}$) line at 22.5 eV, i.e., lower than the expected energy range for satellites. The existence of this satellite is another result of the breakdown of the quasiparticle picture. On a phenomenological basis, all four of the inner-valence-derived satellites appear to be dynamically correlated shake-up states. [S1050-2947(99)02711-0]

PACS number(s): 33.80.Eh

I. INTRODUCTION

Our recent theoretical work on the inner-valence photoionization of acetylene is the first of which we are aware that examines the problem dynamically with inclusion of correlation and multichannel effects [1]. Since this approach yielded interesting results and new insights into the inner-valence photoionization of acetylene, we would like to extend the application of the method to other molecular systems. There were several points to suggest HCN as the next system to study. First, acetylene and HCN are both very important molecules in the envelopes of carbon-rich stars, and as such their photoionization behavior has received attention in astrophysical literature [2–6]. Second, since the two molecules are isoelectronic, HCN represents a system which provides a basis for comparison and contrast with acetylene in terms of its inner valence photoionization dynamics. Finally, because HCN has less symmetry than acetylene, the possibility exists that it would exhibit a more pronounced deviation from the molecular-orbital model of photoionization than the partial breakdown observed with acetylene. Unfortunately it was not possible to gauge the prospects of HCN in this respect because there is insufficient theoretical and experimental data available with which to do so. Although the photoionization of HCN has been well studied in the lower photon energy region up to ~20 eV [7–23], the inner-valence photoionization of HCN has received only cursory attention [13,14,21]. This work then will be a first step in understanding the inner-valence photoionization of HCN.

When the quasiparticle picture of photoionization holds for the inner valence region, there will be an inner-valence main line, the integrated intensity of which will very closely agree (to within $\gtrsim$70%) with that predicted by the Thomas-Reiche-Kuhn sum rule; electron correlation may result in weak satellite features, typically several eV to the high-binding-energy side of the main line in photoelectron spectra that accounts for any remaining intensity that would otherwise reside in the main line. However, in the inner-valence region it is often the case that the inner-valence molecular orbital is quasidegenerate with one or more two-hole–one-particle ($2h$-$1p$) configurations. In this event, final-state correlation may enable a satellite to ''borrow intensity'' from the inner-valence main line, resulting in a significant redistribution of intensity from the main line to the satellite, and in extreme cases, the inner-valence main line intensity may be almost completely redistributed over a number of satellites, some of which may even appear on the low-binding-energy side of the main line [24]. When the inner-valence main line is thus severely diminished or obliterated, we refer to this as the breakdown in the quasiparticle model of photoionization [24–26].

Our previous work on the inner-valence photoionization of acetylene [1] provided an example of the breakdown of the quasiparticle picture of photoionization; the $2\sigma_g^{-1}$ inner-valence line of acetylene loses ~50% of its intensity to the satellite region, up to half of which is borrowed by satellite 2, the $11\,^2\Sigma_g^+$ state. Since most of the acetylene inner-valence intensity still resides in one line, this is only a partial breakdown of the quasiparticle picture of photoionization. With respect to HCN, however, we may *a priori* expect more extreme deviations from the quasiparticle picture. This is because HCN has lower symmetry than acetylene. Therefore, HCN has $2h$-$1p$ configurations resulting from ionization out of the 4σ orbital that are potentially quasidegenerate with the HCN $3\sigma^{-1}$ inner-valence main hole ionization, whereas in acetylene ionization from the analogous orbital, $2\sigma_u$, pro-

*Author to whom correspondence should be addressed.

duces configurations that are symmetry forbidden from mixing with the inner-valence hole state, $2\sigma_g^{-1}$.

In keeping with *a priori* expectations, a central result from the present inner-valence photoionization study predicts that HCN is a molecule exhibiting a complete breakdown of quasiparticle photoionization wherein no single line is definitively identifiable as the inner-valence main line. One implication of this loss of the ''main'' inner-valence line is that it is problematic to analyze the results in terms of the energy-dependent satellite and main cross-section (or experimental intensity) ratios that figure prominently in the phenomenological classification system of Becker and Shirley [27], and also figure prominently from the theoretical standpoint. From a theoretical standpoint, under certain conditions and for reasons we will review in Sec. II at high photon energy the satellite and main ratios (experimental or theoretically derived from cross sections) will approach the corresponding ratio of spectroscopic intensity factors, and this behavior, which we henceforth refer to as convergence, can be used to determine the provenance of the satellite. In other words, convergence occurs when the satellite represents intensity borrowing from the main line to which it is compared. Also in the Becker-Shirley classification system, the satellite and main cross-section ratios can be used to determine what kind of correlation effects contribute to the manifestation of the satellite. We should note that the Becker-Shirley classification system is more commonly applied to situations such as photoionization from core states where the delineation between shake-up states and the main line is not subject to the ambiguity that may exist in inner-valence photoionization. However, an analysis of the present results indicate that assigning a main line is far less of a problem than the problem of overlapping satellite lines, i.e., lines that cannot resolved experimentally, and that any inner-valence line may serve as a main line as long as its provenance is the same as the satellite to which it is compared.

The methodology developed previously for studying the inner-valence photoionization of acetylene is again used here, with apparently excellent results inasmuch as they agree well with the little experimental data available [13,14]. In agreement with the experimental results, we find that there are four satellite lines to the high-binding-energy side of the HCN $4\sigma^{-1}$ main line, and these occur at approximately 22.5, 27.0, 31.0, and 33.0 eV. Additionally, the present results predict another small satellite at *ca*. 2–3 eV above the 27-eV state. The four high-lying states likely result from a predominately $3\sigma^{-1}$ origin, but the lowest satellite at 22.5 eV appears to be of $3\sigma^{-1}$, $4\sigma^{-1}$, and $5\sigma^{-1}$ mixed provenance. In terms of the Becker-Shirley terminology, we illustrate how the four satellites of inner-valence origin are all dynamically correlated shake-up states.

II. THEORY AND COMPUTATIONAL METHODS

The computational methods for the inner-valence work on HCN are similar to those for the inner-valence work on acetylene, and for general details or the calculation we refer the interested reader to this reference and other appropriate references [1,28–30]. To begin this work, we first obtained a set of molecular orbitals from a state-averaged multiconfiguration self-consistent field (MCSCF) [31,32] calculation using the program MOLPRO [33]. The basis set for these calculations was an augmented valence triple-zeta basis (AVTZ) from the MOLPRO library. The HCN geometry used had $C_{\infty v}$ symmetry with $R_{\mathrm{C-N}}=1.153$ Å and $R_{\mathrm{C-H}}=1.066$ Å [34] HCN has the ground-state configuration

$$(1\sigma)^2(2\sigma)^2(3\sigma)^2(4\sigma)^2(5\sigma)^2(1\pi)^4,$$

which in the MOLPRO AVTZ basis set with the above geometry yields a total SCF energy for $X\ ^1\Sigma^+$ of $-92.909\,132$ hartree. The MCSCF calculation performed a state average over fourteen HCN^+ states in which the occupied Hartree-Fock orbitals of HCN were included in the orbital space but were not varied. The MCSCF active space consisted of the HCN ground-state occupied orbitals listed above and a set of virtual orbitals including one orbital of σ symmetry, two orbitals of π symmetry, and one orbital of δ symmetry. The ground-state excitation restrictions allowed a total of two electrons in the virtual active space above 2π, and a total of four electrons in all of the virtual orbitals. Similarly, the ion state excitation restrictions allowed a total of one electron in the virtual active space above 2π and a total of three electrons in all of the virtual orbitals. We varied the number and symmetry of orbitals in the MCSCF active space, and the number and symmetry of states included in the MCSCF state average to arrive at a best MCSCF result within the desired size range of the calculation, a size range dictated by the logistics of the subsequent scattering calculation [30,35].

To determine which states should be included in the MCSCF state average, we first performed several preliminary calculations of spectroscopic intensity factors (SIFs) as a sum of pole strengths according to

$$I^c_{\mathrm{SIF}}=\sum_q I^{q,c}_{\mathrm{SIF}}=\sum_q |x_q^{(c)}|^2, \tag{1}$$

where $I^{q,c}_{\mathrm{SIF}}$ is the contribution of each individual molecular orbital q from which photoionization occurs to the total SIF, c is the final-state channel contributing to the SIF intensity, and $x_q^{(c)}$ is the transition amplitude defined by

$$x_q^{(c)}=\langle \Phi_c^{\mathrm{CI},N-1}|a_q|\Psi_i^{\mathrm{CI},N}\rangle. \tag{2}$$

In Eq. (2), $\Phi_c^{\mathrm{CI},N-1}$ and $\Psi_i^{\mathrm{CI},N}$ are the cth channel $(N-1)$-electron target ion state and N-electron initial-state wave functions, respectively, derived from a numerical configuration interaction calculation (CI, *vide infra*), and a_q is an annihilation operator for an electron in orbital q. The preliminary calculations were based on several sets of orbitals from different MCSCF calculations and the resulting SIF results indicated that, similar to acetylene, the most important satellite states for HCN are those of $^2\Sigma^+$ symmetry. Based on these calculations, 13 of the 14 states included in the MCSCF state average were of $^2\Sigma^+$ symmetry, and the 14th state was of $^2\Pi$ symmetry.

For the inner-valence work on acetylene, there were many experimental and theoretical data available which quantified the binding energies of all of the main lines and the first two satellites fairly closely. Thus, in the case of acetylene we were able to judge the best MCSCF in terms of the ΔE's between the first $^2\Sigma_g^+$ state and three subsequent states of

TABLE I. Numerical CI results using the natural orbitals from the best state-averaged MCSCF calculation on HCN compared to other calculations and experimental data.

	ΔE(eV)		
	$1\ ^2\Sigma^+$ relative to $1\ ^2\Pi$	$2\ ^2\Sigma^+$ relative to $1\ ^2\Pi$	$1\ ^2\Sigma^+$ relative to $2\ ^2\Sigma^+$
MCSCF, this study	0.15	6.85	6.70
MCSTEP[a]	0.04	6.76	6.72
ΔMRSDCI+Q[a]	0.15		
EKT[b]	0.80	8.02	7.22
PES[c]	0.40		
PES[d]	0.40	6.40	6.00

[a]Reference [37], calculated.
[b]Reference [36], calculated.
[c]References [13] and [19].
[d]References [19] and [23].

TABLE II. Ionization potentials from the main lines of HCN obtained from the numerical CI results using the natural orbitals from the best state-averaged MCSCF calculation on HCN compared to other calculations and experimental data

	Ionization potential (eV)		
	$1\ ^2\Pi(1\pi^{-1})$	$1\ ^2\Sigma^+(5\sigma^{-1})$	$2\ ^2\Sigma^+(4\sigma^{-1})$
CI, this study	13.8	13.9	20.6
MCSTEP[a]	13.8	13.8	20.5
ΔMRSDC+Q[a]	13.6	13.8	-
EKT[b]	14.0	14.8	22.0
PES[c]	13.6	14.0	19.1
PES[d]	13.6	14.0	20.0

[a]Reference [37], calculated.
[b]Reference [36], calculated.
[c]References [13] and [19].
[d]References [19] and [23].

that symmetry. In the case of HCN there is not such an experimental and theoretical consensus, and so we judged the best MCSCF on the basis of ΔE's between the three main outer valence lines in comparison to other theory and experiment. Table I compares the values of the ΔEs from the present best MCSCF calculation to experimental photoelectron spectra (PES) [13,19,23] and to other theoretical results computed using the extended Koopman's theorem method [36], the multiconfigurational spin tensor electron propagator method (MCSTE) [37], and the multireference singles and doubles CI with estimated quadruples (ΔMRSDCI+Q) method [37]. The best MCSCF results are not ideal, but are far superior to the other MCSCF calculations that we performed, and are quite good compared to other theoretical results and in light of the experimental uncertainty.

The natural orbitals from the MCSCF calculation served as the starting point for a numerical CI calculation [30] that produces both the N-electron final state and $(N-1)$-electron target ion state wave functions that are used in the scattering calculation. The CI excitation levels are the same as those for the MCSCF; there were up to 1600 symmetry-adapted configuration-state functions (CSF's) for the CI initial states, and up to 660 symmetry-adapted CSF's for the ion states, depending on symmetry. Table II gives main line ionization potentials (IP's) from the CI, along with IP's from the literature. The IP's for each main line are in reasonable agreement with the other estimates in Table II, especially considering the apparent experimental uncertainty in the IP's.

We then examine the SIF's which derive from the best MCSCF orbitals in order to choose ion states for the scattering calculation. By previously developed criteria [1] we have determined that any states which have a large SIF connecting the ion state to the initial ground state should be included in the scattering calculation. Table III lists the $(N-1)$-electron target states for the multichannel scattering calculations, the most important configurations for each target state, the threshold energy of each state, the SIF of each state, and the most important configurations for the ground state, $X\ ^1\Sigma^+$. Regarding the states not listed in Table III, since the next largest SIF is only ~10% of the smallest SIF in Table III, there was a natural delineation of which states to use and which states to reject. Conveniently, this delineation indicated that only eight ion states were required, still a large multichannel calculation, but tractable. The SIF's in Table III are normalized to the number of degenerate electrons per orbital in order to illustrate the main line ''recovery.'' While the $1\pi^{-1}$, $5\sigma^{-1}$, and $4\sigma^{-1}$ SIF's are close to 0.90, the inner valence $3\sigma^{-1}$ is unidentifiable as a single line, and thus in the inner-valence photoionization of HCN we see a complete breakdown of the molecular-orbital picture.

After choosing a set of target ion states based on SIF intensities, a second criterion that we use to determine if any additional target ion states need to be included is the oscillator strength criterion. The eigenfunctions of the N-electron Hamiltonian solved in the space of the CSF's which we obtained using the same orbitals and occupation restrictions used to compute the initial-state CI wave function represent a discretization of the photoionization continuum, and thus approximately represent the resonant and open-channel states that are strongly excited by the photoexcitation of the initial state. We want to make sure that all of these important N-electron states are adequately described by the set of target ion state plus continuum function permutations. To do this, we first evaluate which N-electron excited states are most important by calculating the oscillator strength between the ground-state HCN CI wave function $\Psi_i^{\mathrm{CI},N}$ ($X\ ^1\Sigma^+$), and an N-electron excited-state CI wave function $\Psi_f^{\mathrm{CI},N}$. The oscillator strengths are calculated in the mixed form

$$f_{\mathrm{fi}}^{r,\nabla_r} = \tfrac{2}{3}\langle \Psi_i^{\mathrm{CI},N}|r|\Psi_f^{\mathrm{CI},N}\rangle\langle \Psi_f^{\mathrm{CI},N}|\nabla_r|\Psi_i^{\mathrm{CI},N}\rangle, \qquad (3)$$

where r is the length form transition operator, and ∇_r is the velocity form transition operator. Any N-electron state having an oscillator strength of >0.05 was incorporated into our evaluation of whether the oscillator criterion was met. Table IV gives the percent recovery, as indicated by the normalized projection of the final state onto the target plus molecular-orbital penetration terms, of the N-electron initial states having significant oscillator strengths by the set of $(N-1)$-electron ion states in Table III. Optimally the recovery in Table IV should be ≥ 0.90, but in the case of $12\ ^1\Sigma^+$ we could not identify further ion states which, upon inclusion

TABLE III. HCN N-electron ground state and $(N-1)$-electron ion states used in multichannel scattering calculation.

State	Energy above ground state, eV	SIF[a]	Important configurations[b]
N-electron ground state			
$X\ ^1\Sigma^+$	0.00	NA	0.95 ground state $0.23(1\pi)^{-2}(2\pi)^2$
$(N$-1)-electron target states			
$1\ ^2\Pi(1\pi^{-1})$	13.82	0.90	$0.94(1\pi)^{-1}$ $0.19(1\pi)^{-3}(2\pi)^2$ $0.16(1\pi)^{-2}(2\pi)^1$
$1\ ^2\Sigma^+(5\sigma^{-1})$	13.88	0.85	$0.90(5\sigma)^{-1}$ $0.28(5\sigma)^{-1}(1\pi)^{-1}(2\pi)^1$ $0.19(5\sigma)^{-1}(1\pi)^{-2}(2\pi)^2$
$2\ ^2\Sigma^+(4\sigma^{-1})$	20.61	0.84	$0.88(4\sigma)^{-1}$ $0.21(5\sigma)^{-1}(1\pi)^{-1}(2\pi)^1$ $0.21(4\sigma)^{-1}(1\pi)^{-2}(2\pi)^2$ $0.20(4\sigma)^{-1}(1\pi)^{-1}(3\pi)^1$ $0.21(4\sigma)^{-1}(1\pi)^{-1}(2\pi)^1$
$3\ ^2\Sigma^+$	22.81	0.083	$0.87(5\sigma)^{-1}(1\pi)^{-1}(2\pi)^1$ $0.24(5\sigma)^{-1}(1\pi)^{-2}(2\pi)^2$ $0.19(4\sigma)^{-1}$ $0.16(3\sigma)^{-1}$ $0.15(5\sigma)^{-1}(1\pi)^{-2}(2\pi)^1(3\pi)^1$ $0.15(5\sigma)^{-1}$
$6\ ^2\Sigma^+$	27.79	0.226	$0.76(4\sigma)^{-1}(1\pi)^{-1}(2\pi)^1$ $0.45(3\sigma)^{-1}$ $0.18(5\sigma)^{-1}(1\pi)^{-1}(2\pi)^1$ $0.15(4\sigma)^{-1}(1\pi)^{-2}(2\pi)^1(3\pi)^1$
$9\ ^2\Sigma^+$	30.41	0.083	$0.63(5\sigma)^{-1}(1\pi)^{-2}(2\pi)^2$ $0.37(5\sigma)^{-1}(1\pi)^{-1}(2\pi)^1$ $0.36(1\pi)^{-2}(6\sigma)^1$ $0.28(3\sigma)^{-1}$ $0.25(4\sigma)^{-1}(1\pi)^{-1}(2\pi)^1$ $0.22(5\sigma)^{-2}(6\sigma)^1$
$13\ ^2\Sigma^+$	32.29	0.255	$0.48(3\sigma)^{-1}$ $0.43(5\sigma)^{-1}(1\pi)^{-2}(2\pi)^2$ $0.40(4\sigma)^{-1}(1\pi)^{-1}(2\pi)^1$ $0.32(5\sigma)^{-1}(1\pi)^{-1}(2\pi)^1$ $0.29(1\pi)^{-2}(6\sigma)^1$ $0.19(4\sigma)^{-1}(5\sigma)^{-1}(6\sigma)^1$
$14\ ^2\Sigma^+$	33.44	0.279	$0.56(5\sigma)^{-1}(1\pi)^{-1}(2\pi)^1$ $0.48(3\sigma)^{-1}$ $0.39(5\sigma)^{-1}(1\pi)^{-2}(2\pi)^2$ $0.27(4\sigma)^{-1}(5\sigma)^{-1}(6\sigma)^1$ $0.19(5\sigma)^{-1}(1\pi)^{-1}(3\pi)^1$ $0.16(3\sigma)^{-1}(1\pi)^{-2}(2\pi)^2$ $0.15(4\sigma)^{-1}(1\pi)^{-2}(2\pi)^2$

[a]Normalized by dividing by the number of degenerate electrons in orbital, 4 for π, 2 for σ.
[b]Absolute values of CI coefficients.

into the target ion state list, improved this recovery. Because the state has a very weak oscillator strength, i.e., is not likely to be a very important N-electron excited state, and because the recovery of this state in Table IV is still quite reasonable at 0.75, we continued the calculation without adding any further target ion states to the set listed in Table III.

A final consideration before performing the scattering calculation is to avoid the phenomenon of overcompleteness [28,38]. One manner by which overcompleteness may be avoided is to impose orthogonality constraints which preclude the inclusion of linear dependencies in the multichannel CI wave function expansion used in the scattering calculation. For the inner-valence calculation on HCN we found that it was sufficient to orthogonalize the continuum scattering functions to the strongly occupied molecular orbitals, and no other orthogonality constraints were necessary. We veri-

TABLE IV. *N*-electron excited states used in choosing ion states for multichannel scattering calculation on HCN.

Excited-state Symmetry	Energy above ground state (eV)	Oscillator strength	Fraction of initial state recovered by penetration terms
$5\ ^1\Sigma^+$	15.90	0.07	0.97
$6\ ^1\Sigma^+$	17.75	0.65	0.98
$7\ ^1\Sigma^+$	18.57	0.45	0.97
$10\ ^1\Sigma^+$	22.70	0.43	0.97
$12\ ^1\Sigma^+$	23.68	0.05	0.75
$18\ ^1\Sigma^+$	27.00	0.07	0.91

fied this by calculating the eigenvalues of the overlap matrix for the target plus molecular-orbital penetration terms.

After arriving at a suitable list of ion states, and determining that no special orthogonality constraints were necessary, we performed both single-channel and multichannel scattering calculations to determine the photoionization cross sections for HCN over the photon energy range of 40–1000 eV; in the course of this work, we also calculated photoionization asymmetry parameters [39], but will not report these here as they do not enter into the discussion below. Since the scattering calculations have been described in great detail previously [28,30,40,41], we will only briefly review them here. In the study of photoionization we only need to calculate matrix elements of one-electron operators between the initial- and final-state wave functions. We calculate multichannel (MC) or single-channel (SC) photoionization cross sections using a Schwinger variational method that determines photoionization cross sections in the mixed form. Photoionization cross sections are given by

$$\sigma_c^{\mathrm{MC(SC),mixed}} = \sum_S \frac{4\pi^2}{3} \langle \Psi_{s,c,f}^{\mathrm{MC(SC)CI,N}} | r | \Psi_i^{\mathrm{CI},N} \rangle \times \langle \Psi_i^{\mathrm{CI},N} | \nabla_r | \Psi_{s,c,f}^{\mathrm{MC(SC)CI,N}} \rangle, \tag{4}$$

where in a neutral system of N electrons one of the electrons is not bound. The one-electron continuum functions are explicitly incorporated into the electronic multichannel or single-channel configuration-interaction (MCCI or SCCI) scattering function, $\Psi_{S,f}^{\mathrm{MCCI},N}$, such that

$$\Psi_{s,c,f}^{\mathrm{MCCI},N} = \sum_{c'=1}^{N_c} \Phi_{c'}^{\mathrm{CI},N-1}(\chi_{c',c,S}) = \sum_{c'=1}^{N_c} \sum_{i=1}^{N_b} \psi_i(\chi_{c',c,S}) C_{ic'}, \tag{5a}$$

and

$$\Psi_{S,j}^{\mathrm{SCCI},N} = \Phi_c^{\mathrm{CI},N-1}(\chi_{c,c,S}) = \sum_{i=1}^{N_b} \psi_i(\chi_{c,c,S}) C_{i,c}. \tag{5b}$$

In Eqs. (4) and (5) the index S indicates the asymptotic boundary condition for ionization leading to the cth ion state, the index f indicates a final scattering state, N_c is the number of channels, $\chi_{c',c,S}$ is the c'th channel one-electron continuum function, N_b is the number of CSFs, ψ_i is an $(N-1)$-electron CSF, and $C_{ic'}$ are expansion coefficients for the expansion of $\Phi_{c'}^{\mathrm{CI},N-1}$. The notation $\Phi_{c'}^{\mathrm{CI},N-1}(\chi_{c',c,S})$ is an antisymmetrized spin- and symmetry-adapted N-electron final-state function constructed from the product of the c'th channel target ion state $\Phi_{c'}^{\mathrm{CI},N-1}$ and the continuum state $\chi_{c',c,S}$; similarly, the notation $\psi_i(\chi_{c',c,S})$ is an antisymmetrized spin- and symmetry-adapted N-electron CSF constructed from the product of ψ_i and $\chi_{c',c,S}$.

The Lippman-Schwinger equations gives the functions $\chi_{c',c,S}$ through

$$\underline{\chi_{c,S}} = \underline{\chi_{c,S}^{(0)}} + \underline{\underline{G}}\,\underline{\underline{V}}\ \underline{\chi_{c,S}}, \tag{6a}$$

where $\underline{\chi_{c,S}}$ is a length N_c vector of components $\chi_{c',c,S}$, $\underline{\chi_{c,S}^{(0)}}$ is a length N_c vector whose components are all zero except for the one which is the continuum function in the absence of the scattering potential for the asymptotic state S in channel c, $\underline{\underline{G}}$ is a diagonal matrix of Coulomb Green's functions, and $\underline{\underline{V}}$ is the potential matrix. The potential V has the form of a Phillips-Kleinman pseudopotential [42], and the multichannel Coulomb Green's-function matrix is

$$(\underline{\underline{G}}) = (\underline{\underline{G}})_{cc'} G(E_c)\, \delta_{cc'}, \tag{6b}$$

where G is the Coulomb Green's function,

$$G(E_c) = \lim_{\varepsilon \to 0} \left(-\frac{1}{2}\nabla^2 - \frac{1}{r} - E_c - i\varepsilon \right)^{-1}, \tag{6c}$$

E_c is the asymptotic energy of the electron leaving the molecule in target state c, and δ is the Kronecker delta.

As noted in Sec. I previous theoretical works [1,24,43] have described how, under certain conditions, the expression

$$\frac{\sigma_{c'}}{\sigma_c} = \frac{I_{\mathrm{SIF}}^{c'}}{I_{\mathrm{SIF}}^{c}} \tag{7}$$

is valid. Equation (7) may only be true under the following conditions: (1) At photon energies high enough to be in the sudden limit, or, in other words, when the photoionized electron leaves with sufficient energy that the residual target ion state orbitals do not have time to relax during the process. (2) When interchannel coupling and nonorthogonality terms [24] are negligible. (3) When the photoionization process is dominated by a single orbital. (4) When the photoionization matrix elements for states c and c' are similar and the energy dependences of both are weak. The second and fourth conditions above are generally believed to be true at high photon energy [24]. In the event that Eq. (7) is valid it implies that the provenance of a satellite state c' can be assigned to the main line c and provides a form of correspondence between static theory (energy-independent SIF's) and dynamic theory (energy-dependent photoionization cross sections). However, even in cases where Eq. (7) is invalid, the energy-dependent cross section ratio can still be used to study the effects of correlation on satellite states per Becker and Shirley.

III. RESULTS AND DISCUSSION

A. Photoionization cross sections

The high-energy behavior of photoionization cross sections can be qualitatively understood by approximating the continuum function in the dipole matrix element, which de-

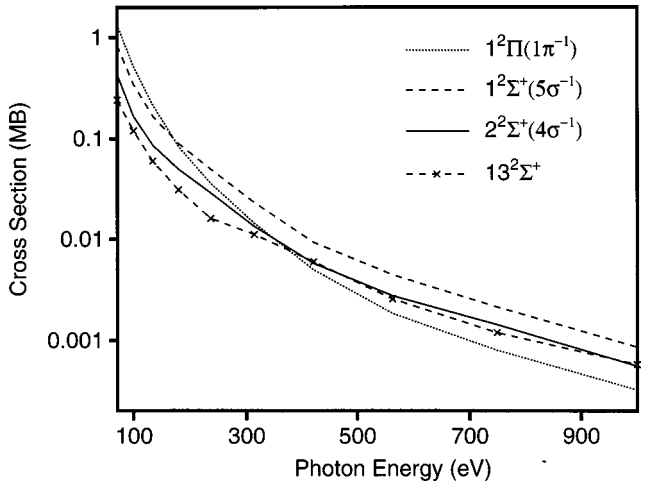

FIG. 1. Total multichannel cross sections for main-line channels of HCN as a function of photon energy.

termines the cross section, by a plane wave. Then the energy dependence of the cross section can be seen to be determined by the momentum distribution of the hole orbital. In general an *s* orbital has more high-momentum components than the corresponding *p* orbital coming from the same atomic shell. Thus the cross section for ionizing out of an *s* orbital will decrease more slowly at high energy than does the cross section for the corresponding *p* orbital. Additionally, one would expect that as atoms with higher *Z* are considered the cross sections from the same orbital would also decrease at a slower rate at high photon energy compared to the cross sections for atoms of lower *Z*. These qualitative expectations are in agreement with the atomic photoionization cross section for the C and N atoms. The cross sections for both C and N 2*p* orbitals are much smaller at high energy than the cross sections for either C or N 2*s*. Additionally, the cross section for N 2*p* is ~3 times that of C 2*p* at 1040 eV and the cross section of N 2*s* is ~2 times that of C 2*s* at the same energy [44]. The high-energy behavior of the photoionization from a given molecular orbital can then be understood qualitatively by considering the behavior of the orbital near the nuclei. In a linear-combination-of-atomic-orbital representation of a molecular orbital, the expansion coefficients can be used to qualitatively estimate the relative *s* and *p* content of a molecular orbital at a given center, and thus to understand its high-energy photoionization cross section behavior.

Figure 1 shows the total multichannel cross section for the main line channels $1\ ^2\Pi(1\pi^{-1})$, $1\ ^2\Sigma^+(5\sigma^{-1})$, and $2\ ^2\Sigma^+(4\sigma^{-1})$ as well as the multichannel cross section for the channel $13\ ^2\Sigma^+$, the latter of which has CSF's that are most strongly dominated by the inner valence $3\sigma^{-1}$, per Table III. Although the outer valence $1\ ^2\Pi(1\pi^{-1})$ is decreasing very rapidly with energy as compared to $2\ ^2\Sigma^+(4\sigma^{-1})$ and $13\ ^2\Sigma^+$, the $1\ ^2\Sigma^+(5\sigma^{-1})$ outer-valence cross section does not decrease with the same rapidity as a function of photon energy as the analogous $1\ ^2\Sigma_g^+(3\sigma_g^{-1})$ did for acetylene. In isoelectronic acetylene, molecular-orbital coefficients show that the $3\sigma_g$ orbital is considerably more *p* like than the inner valence $2\sigma_g$ orbital, and so the cross section for $1\ ^2\Sigma_g^+$ drops more rapidly than $2\ ^2\Sigma_g^+$ at high photon energy. The HCN molecular-orbital coefficients show that $5\sigma^{-1}$, $4\sigma^{-1}$, and $3\sigma^{-1}$ all have a reasonable

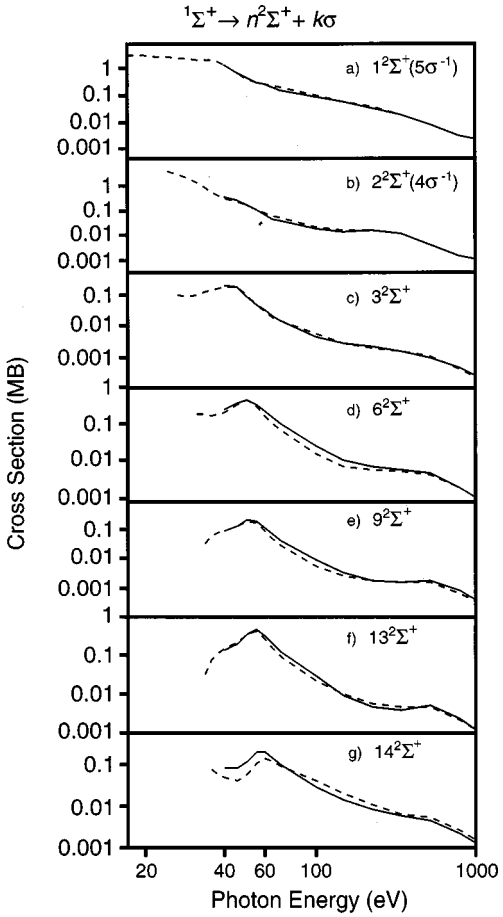

FIG. 2. Single-channel (dashed line) and multichannel (solid line) cross sections for the $^1\Sigma^+ \rightarrow n\ ^2\Sigma^+ + k\sigma$ continua of the main line and most significant $^2\Sigma^+$ satellite channels. (a) $1\ ^2\Sigma^+(5\sigma^{-1})$. (b) $2\ ^2\Sigma^+(4\sigma^{-1})$. (c) $3\ ^2\Sigma^+$. (d) $6\ ^2\Sigma^+$. (e) $9\ ^2\Sigma^+$. (f) $13\ ^2\Sigma^+$. (g) $14\ ^2\Sigma^+$.

amount of *p*-like character as well as *s*-like character. Since the HCN 5σ orbital has substantial N 2*s* and 2*p* character, the qualitative model discussed above agrees with the fact that the $5\sigma^{-1}(1\ ^2\Sigma^+)$ cross section for HCN falls off less rapidly at high photon energies than did $3\sigma_g^{-1}(1\ ^2\Sigma_g^+)$ for acetylene.

A thorough scrutiny of the HCN inner-valence photoionization requires an understanding of the cross-section behavior of the $^2\Sigma^+$ states. Figures 2(a)–2(g) and 3(a)–3(g) show the partial-channel cross sections for all of the $^2\Sigma^+$ states in this study. The first item of general note about both figures is that the difference between the single-channel and multichannel cross sections is not very pronounced at any photon energy. Those channels which do exhibit minor differences are satellites, and, inasmuch as satellites are sometimes referred to as correlation states, it makes sense that these states would be more likely to exhibit correlation effects. On the other hand, it is surprising that the minor differences between the single-channel and multichannel results in Figs. 2 and 3 occur in the intermediate photon energy range, and that the agreement between the single-channel and multichannel results is good in the lower photon energy range. As compared to our previous work on acetylene, the MCCI scattering function in this calculation is constructed in the same manner. However, the active space used in the present MC-

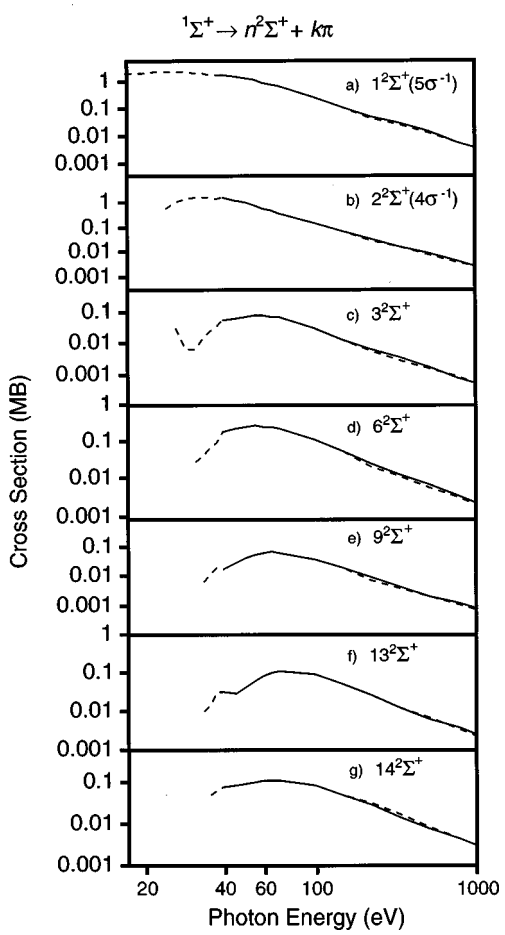

FIG. 3. Single-channel (dashed line) and multichannel (solid line) cross sections for the $^1\Sigma^+ \rightarrow n\ ^2\Sigma^+ + k\pi$ continua of the main line and most significant $^2\Sigma^+$ satellite channels. (a) $1\ ^2\Sigma^+(5\sigma^{-1})$. (b) $2\ ^2\Sigma^+(4\sigma^{-1})$. (c) $3\ ^2\Sigma^+$. (d) $6\ ^2\Sigma^+$. (e) $9\ ^2\Sigma^+$. (f) $13\ ^2\Sigma^+$. (g) $14\ ^2\Sigma^+$.

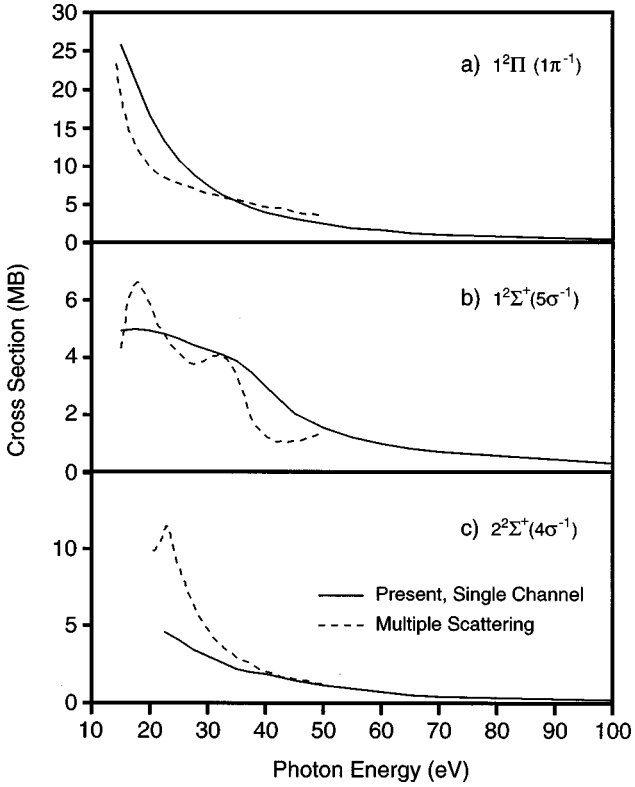

FIG. 4. Present single-channel HCN cross-section results compared to the multiple, scattering results of Ref. [21]. (a) $1\ ^2\Pi(1\pi^{-1})$. (b) $1\ ^2\Sigma^+(5\sigma^{-1})$. (c) $2\ ^2\Sigma^+(4\sigma^{-1})$.

SCF calculation is smaller than the active space used in the acetylene calculation, which reduces the amount of correlation associated with the initial and target ion states. Since the main difference between the single-channel and multichannel results is that the latter incorporate interchannel coupling, we may interpret the similarity between the two sets of data in Figs. 2 and 3 as an indication that interchannel coupling is not significant in this calculation.

In discussing Table III, we remarked that the SIFs and important CSFs for the states above $2\ ^2\Sigma^+$ indicate a complete breakdown of molecular-orbital photoionization. As a result, we cannot unambiguously identify a $3\sigma^{-1}$ ''line.'' This makes the assessment of the satellite structures quite a bit more challenging. For instance, on the basis of the energy dependent behavior of the $4\sigma^{-1}(2\ ^2\Sigma^+)$ and $5\sigma^{-1}(1\ ^2\Sigma^+)$ cross sections we might be able to identify contributions from these to the energy-dependent behavior of the satellite cross sections. However, $3\sigma^{-1}$ must also certainly be a large contributor to the satellite cross sections, but since there is no ''main line'' for $3\sigma^{-1}$ it is impossible to assign inner valence contributions to the satellites on the basis of the $3\sigma^{-1}$ energy-dependent behavior, i.e., the approach used in the inner valence study on acetylene. We will return to this point later. For now, it remains to complete our examination of the partial-channel cross-section behavior. In Figs. 2(a), 2(b), 3(a), and 3(b), we see that the main line cross sections have no structure in the range of interest above 40 eV, and decrease steadily with increasing photon energy. There are some oscillatory structures at photon energies above 100 eV in the $^1\Sigma^+ \rightarrow {}^2\Sigma^+ + k\sigma$ channels which have been previously characterized in other systems [1,45], and which result from energy-dependent variations in the contribution from various components of angular momenta to the cross section. For the satellite cross sections in Figs. 2(c), 2(d), and 2(g), there is a structure in the $^1\Sigma^+ \rightarrow {}^2\Sigma^+ + k\sigma$ cross section which occurs at approximately 22 eV above threshold and is probably a high-energy shape resonance. The shape of the $^1\Sigma^+ \rightarrow {}^2\Sigma^+ + k\sigma$ cross section in the 30–70-eV region in Figs. 2(e) and 2(f) suggests that there may be an additional shape resonance at approximately 9 eV above threshold. The $^1\Sigma^+ \rightarrow {}^2\Sigma^+ + k\pi$ satellite cross sections in Figs. 3(c)–3(g) also indicate an additional structure not apparent in the main lines; this structure is manifested as a dip near ~30 eV in the $^1\Sigma^+ \rightarrow {}^2\Sigma^+ + k\pi$ cross section in Fig. 3(c) ($3\ ^2\Sigma^+$), which, given the shape of the structure and the complex provenance of $3\ ^2\Sigma^+$ in Table III, is probably an interference effect arising when the various contributing functions have phases that do not vary at the same rate.

Figures 4(a)–4(c) compare the total HCN $1\ ^2\Pi$, $1\ ^2\Sigma^+$, and $2\ ^2\Sigma^+$ cross sections from the present single-channel calculation to those from Ref. [21], which were calculated using the multiple-scattering model. Generally, our results are in reasonable agreement with theirs, both qualitatively and quantitatively. However, one disadvantage of the multiple-scattering method is that resonances in the cross

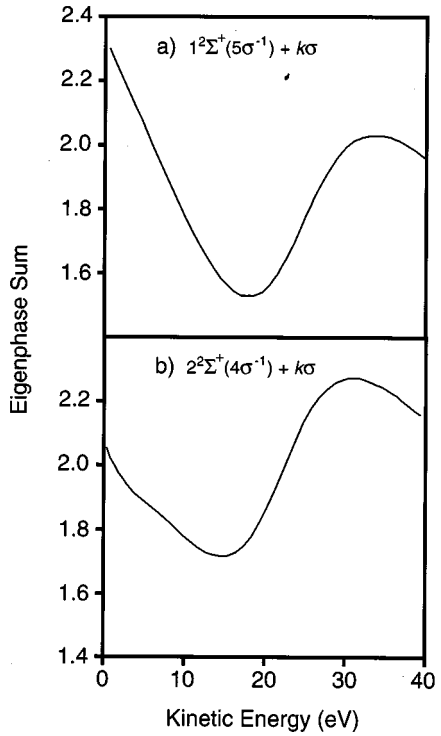

FIG. 5. Single-channel eigenphase sums for electron-ion scattering off of two main line hole states of HCN as a function of the kinetic energy of the scattered electron. (a) $1\ ^2\Sigma^+(5\sigma^{-1})+k\sigma$. (b) $2\ ^2\Sigma^+(4\sigma^{-1})+k\sigma$.

section are often unrealistically narrow (compare, for instance, work on N_2 by Stephens and Dill [46], Basden and Lucchese [47], Lucchese and Zurales [35], and Poliakoff, Kakar, and Resenberg [48]). Thus the results of Ref. [21] show two strong resonances in Fig. 4(b) and one strong resonance in Fig. 4(c), which are considerably more distinct than what the present results indicate. Also, in Fig. 4(c) the present results indicate a small structure at ~40-eV photon energy which is not apparent in the results of Ref. [21].

Both Ref. [21] and the present study indicate that there may be one or more shape resonances appearing in the $^2\Sigma^+$ channels. If there is such a resonance, it should be reflected by a rise in the eigenphase sum. Figures 5(a) and 5(b) show the eigenphase sums for $1\ ^2\Sigma^+$ and $2\ ^2\Sigma^+$, respectively, confirming this rise. A Breit-Wigner fit of these results indicates that there is one shape resonance which appears at 24.7 eV above threshold in $1\ ^2\Sigma^+$ and 22.7 eV above threshold in $2\ ^2\Sigma^+$, with widths of 16.0 and 16.7 eV, respectively, in each channel; this shape resonance contributes to the structure in the other $^2\Sigma^+$ channels.

B. Dynamic vs static theoretical treatment of satellites

Table V lists the orbital contributions to the SIF intensity for each $^2\Sigma^+$ channel. These data indicate that the two $^2\Sigma^+$ main lines, $1\ ^2\Sigma^+$ and $2\ ^2\Sigma^+$, derive most of their intensity from $5\sigma^{-1}$ and $4\sigma^{-1}$, respectively, in keeping with the quasiparticle picture. Other than $3\ ^2\Sigma^+$, which is an amalgam of $5\sigma^{-1}$, $4\sigma^{-1}$, and $3\sigma^{-1}$, Table V suggests that the remaining satellites derive most of their intensity from $3\sigma^{-1}$. The relative contributions of $5\sigma^{-1}$ and $4\sigma^{-1}$ to the satellites does vary somewhat among the satellites, however, since the

TABLE V. Orbital contributions to SIF intensity for HCN.

	Source of SIF intensity (%)			
Channel	3σ	4σ	5σ	6σ
$1\ ^2\Sigma^+$	0.10	0.10	99.73	0.06
$2\ ^2\Sigma^+$	0.05	99.05	0.89	0.01
$3\ ^2\Sigma^+$	31.47	45.67	22.87	1.67
$6\ ^2\Sigma^+$	93.24	4.62	1.80	0.34
$9\ ^2\Sigma^+$	90.16	1.96	7.78	0.10
$13\ ^2\Sigma^+$	92.54	4.70	2.64	0.12
$14\ ^2\Sigma^+$	90.39	2.28	6.93	0.39

energy dependence of $1\ ^2\Sigma^+$ and $2\ ^2\Sigma^+$ are similar, there is not any immediate avenue for assessing the relative importance of these contributions.

Convoluting the SIF pole strengths with Gaussian functions produces a simulated PES. The resulting simulated spectrum is in Fig. 6(a) and Figs. 6(b)–6(e) show a series of simulated spectra from convoluting photoionization cross sections with Gaussian functions. The cross-section-based spectra are simulated for photon energies of 1000, 100, 70, and 40 eV, respectively. For the sake of comparison, the vertical axis in Fig. 6 represents intensity relative to the $6\ ^2\Sigma^+$ state. The four simulated spectra in Figs. 6(b)–6(e) illustrate how the predicted HCN PES changes with increasing photon energy. At 40 eV, most of the satellite intensity is in $6\ ^2\Sigma^+$. By 70 eV there has been a shift, and now most of the intensity is in $13\ ^2\Sigma^+$. From 70 to 1000 eV the satellites with energies above $6\ ^2\Sigma^+$ continue to increase in relative intensity, with a gradual redistribution of intensity to higher photon energy. In particular, $14\ ^2\Sigma^+$ acquires a significant intensity by 1000 eV, relative to the other satellites.

The energy-dependent behavior of $3\ ^2\Sigma^+$ is quite different from the other satellites in Fig. 6, as we might expect from what we know of its provenance in Table V. The intensity of this satellite varies with the relative intensity of $2\ ^2\Sigma^+(4\sigma^{-1})$, as apparent from the tail of the latter which is in the low photon energy region of the simulated PES in Figs. 6(b)–6(e). If we think about the origins of $3\ ^2\Sigma^+$ in light of the inner-valence photoionization of acetylene [1], we can say that $3\ ^2\Sigma^+$ arises in part as a result of the lower symmetry of HCN as compared to acetylene. For the analogous satellite to exist in acetylene, it would have to be a mixture of $1\ ^2\Sigma_g^+(3\sigma_g^{-1})$, $1\ ^2\Sigma_u^+(2\sigma_u^{-1})$, and $2\ ^2\Sigma_g^+(2\sigma_g^{-1})$; since this mixed provence is symmetry forbidden in acetylene, we do not see any low binding energy acetylene satellite analogous to $3\ ^2\Sigma^+$. Thus for HCN we are able to observe one of the hallmarks of the breakdown of the quasiparticle model [24], that is, we observe a satellite band in the binding-energy region which we normally think of as the outer-valence region.

Returning to the consideration of static theoretical results (SIFs) in Fig. 6(a), we see that these results agree rather well with the cross-section-based simulated PES spectrum at 1000 eV. At 1000 eV, the simulated spectrum in Fig. 6(b) is at the sudden limit. This means that as the photoionized electron leaves the molecule too suddenly for the residual target ion to relax during the exit process. If we look at the Eq. (2) expression for the transition amplitude, a quantity that is

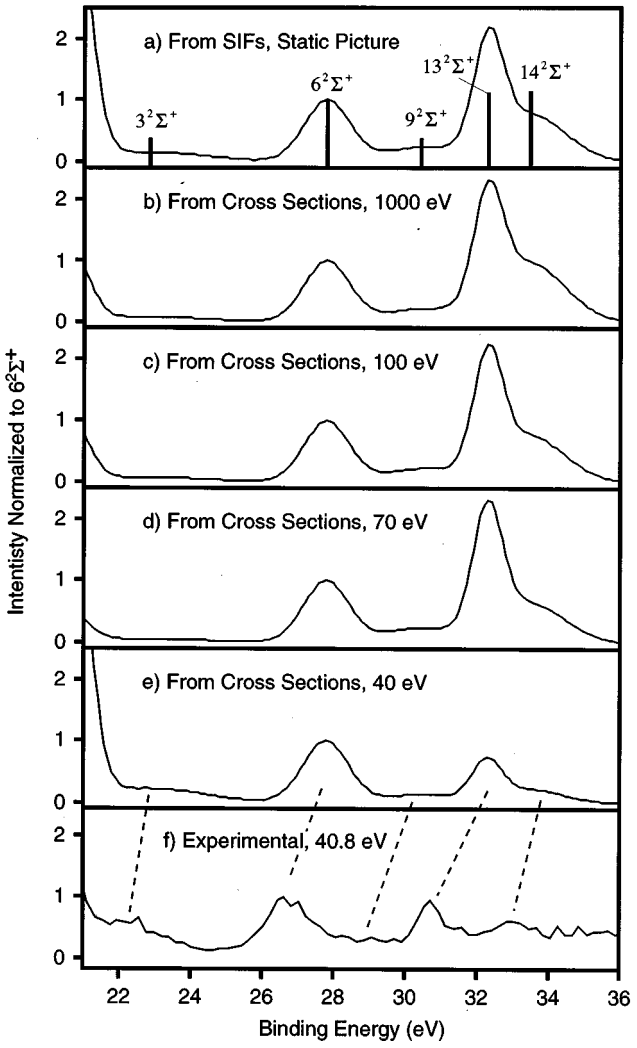

FIG. 6. SIF results, simulated PES spectra, and a He II experimental spectrum for the satellite region of HCN. All results are given without any binding-energy corrections. Simulated spectra are constructed by convolution of the cross-section magnitude or SIF magnitude with peak widths fitted from experimental data. (a) SIF pole strengths and simulated PES spectrum based on SIF's. Simulated PES spectrum based on cross sections at a photon energy of (b) 1000 eV, (c) 100 eV, (d) 70 eV, and (e) 40 eV. (f) Experimental spectrum at a photon energy of 40.8 eV from Eland *et al.* [Ref. [14]].

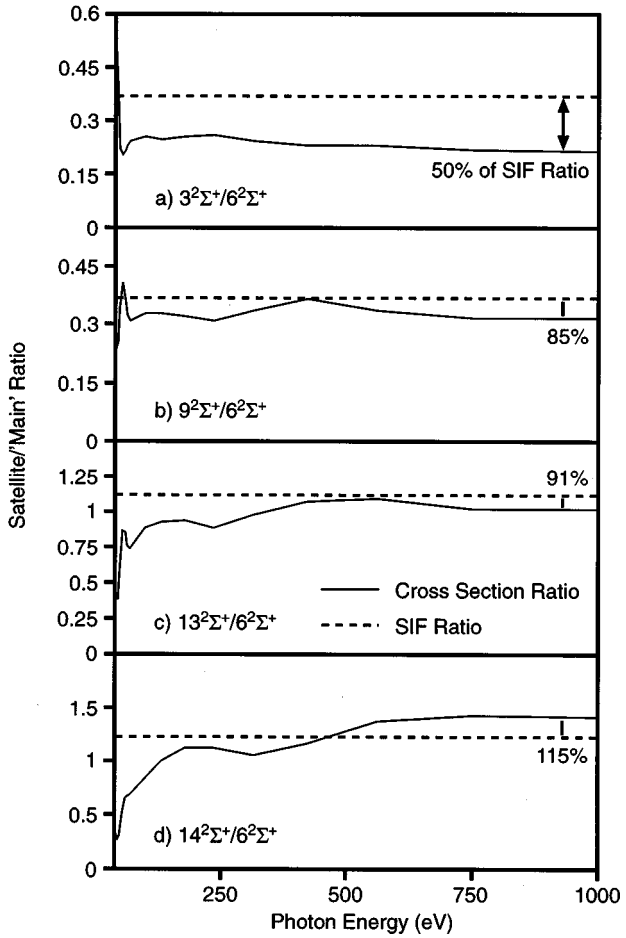

FIG. 7. Photon energy dependence of multichannel $n\ ^2\Sigma^+/6\ ^2\Sigma^+$ cross-section ratios compared to the corresponding SIF ratio, $I_{\mathrm{SIF}}^{n^2\Sigma^+}/I_{\mathrm{SIF}}^{6^2\Sigma^+}$. States used for the numerator in the ratios are (a) $3\ ^2\Sigma^+$, (b) $9\ ^2\Sigma^+$, (c) $13\ ^2\Sigma^+$, and (d) $14\ ^2\Sigma^+$.

used to calculate the pole strengths that go into the SIFs, the ket in this expression describes a set of $(N-1)$-electron unrelaxed orbitals. This is the reason why we may reasonably expect that simulated spectra based on static theoretical results should resemble results from dynamic theory at high energies in the sudden limit.

There is little experimental data on HCN with which to compare the simulated spectra in Figs. 6(b)–6(e), and Fig. 6(f) is the only experimental PES spectrum of which we are aware that clearly resolves the satellite region of HCN [14]. The He II PES in Fig. 6(f) is in good agreement with the 40-eV photon energy simulated spectrum in Fig. 6(e). Note that the simulated PES in Fig. 6(e) shows that in our calculations the ionization potentials are consistently about 1 eV higher that the experimental ionization potentials. We also note that the relative intensities are in good agreement with those found in the experiment.

The next step in analyzing the dynamic data in Fig. 6 is to look at the satellite energy dependence as described by the phenomenological approach of Becker and Shirley [27]. The problem is that this approach for examining satellites involves designating a parent peak, or main line. The two most obvious choices for a ''main'' inner-valence line are $6\ ^2\Sigma^+$ and $13\ ^2\Sigma^+$. The first is a reasonable choice since it is the lowest-binding-energy satellite for which both the SIF's in Table V and the CSF's in Table III indicate a substantial amount of $3\sigma^{-1}$ character. The second, however, carries the bulk of the satellite intensity even at 70 eV [Fig. 6(d)] and is the only satellite for which the principle CSF is the $3\sigma^{-1}$ hole state configuration. Figures 7(a)–7(d) show the satellite/main ratios where $6\ ^2\Sigma^+$ serves as the main line. The cross-section ratios in Figs. 7(b)–7(d) are all within 15% of the corresponding SIF ratios. Also, the shape of each cross-section ratio profile in Figs. 7(b)–7(d) suggests that the cross-section ratios are converging to the corresponding SIF ratio. Since all of the states used in Figs. 7(b)–7(d) are satellites which have $3\sigma^{-1}$ hole state CSF contributions and no contributions from $4\sigma^{-1}$ or $5\sigma^{-1}$ CSF's, this observation may represent convergence. We observed previously how

the static picture from the SIF's indicates that there should be $4\sigma^{-1}$ and/or $5\sigma^{-1}$ contributions to all of the satellites; thus this convergence behavior illustrates once again how the static and dynamic view of photoionization can sometimes be at odds. One reason why $4\sigma^{-1}$ and $5\sigma^{-1}$ contributions might not interfere with the convergence behavior of satellites in HCN is that the cross sections of the HCN main lines do not appear to have the kind of very different energy-dependent behavior that we observed for the main lines in acetylene. In acetylene, the $2\sigma_g^{-1}$ cross section decreases much less rapidly at high energy than the $3\sigma_g^{-1}$ cross section, and as a result a small contribution of $2\sigma_g^{-1}$ to the $18\ ^2\Sigma_g^+$ state caused this state to behave unlike the $3\sigma_g^{-1}$ main line from which originated.

In contrast to the ratios $9\ ^2\Sigma^+/6\ ^2\Sigma^+$, $13\ ^2\Sigma^+/6\ ^2\Sigma^+$, and $14\ ^2\Sigma^+/6\ ^2\Sigma^+$, the cross section ratio for $3\ ^2\Sigma^+/6\ ^2\Sigma^+$, in Fig. 7(a) has approached a constant value at high photon energy, but this ratio at 1000 eV is ~50% of the SIF ratio. This suggests that the ratio of the satellite to main cross sections for $3\ ^2\Sigma^+$, a satellite with a mixed hole state provenance, is nonconvergent as a result of the mixed provenance. Also, in comparing Figs. 7(b)–7(d) with Fig. 7(a), we see how this mixed provenance compares with other cases ($9\ ^2\Sigma^+$, $13\ ^2\Sigma^+$, and $14\ ^2\Sigma^+$) where there is apparent convergence, and where both the SIF's and CSF's indicate only small contributions from $4\sigma^{-1}$ and $5\sigma^{-1}$ main lines.

We mentioned that in the case of HCN there are at least two logical choices for the main line, and that $13\ ^2\Sigma^+$ might also serve in examining the energy dependence of satellite states per the Becker-Shirley approach. At some point, the question arises of how this approach might be extended in cases of even more drastic splitting of the inner-valence line. To pursue this idea we considered all possible permutations of ratios for $6\ ^2\Sigma^+$, $9\ ^2\Sigma^+$, $13\ ^2\Sigma^+$, and $14\ ^2\Sigma^+$, and compared the cross section ratios at 1000 eV to the corresponding SIF ratios. The cross-section ratio for all of the possible main line choices differs from the SIF ratio by an average of 17%. In contrast, the satellite to main cross-section ratios and SIF ratios using all permutations of $6\ ^2\Sigma^+$, $9\ ^2\Sigma^+$, $13\ ^2\Sigma^+$, and $14\ ^2\Sigma^+$ as satellites and $1\ ^2\Pi$, $1\ ^2\Sigma^+$, and $2\ ^2\Sigma^+$ as the main lines results in a cross-section ratio that is on average 742% of the corresponding SIF ratio. Thus it appears that the cross-section ratios in Figs. 7(a)–7(d) are converging to the SIF ratio, and that this convergent behavior may occur even if a low intensity line such as $9\ ^2\Sigma^+$ is used as the main line, as long as the two lines designated as the satellite and main have the same provenance.

Note that the binding energies in Table III and the spectra in Fig. 6 all suggest that, unlike the acetylene satellite region, the states identified here can each be considered as individual satellites, and hence the ratios in Figs. 7 should be directly comparable to experimental data. This is an important point. A theorist obtains separate lines from a calculation by which data can be viewed either in terms of Eq. (7) or in terms of the Becker-Shirley system. Conversely, treatment of experimental data by either approach is problematic if one or more lines overlap and cannot be resolved. One work [49] addressed this problem by comparing experimental satellite to main intensity ratios to SIF ratios, per Eq. (7), and, because the theoretical results in that study indicated that several lines contributed to each satellite, the SIF's of the lines contributing to each satellite were summed in the numerator of the expression. Inasmuch as no sum appears in the numerator of Eq. (7), this summing negates the possibility of observing convergence of the intensity ration to the SIF ratio, except serendipitously. Since HCN appears to be an excellent prospect for the experimental study of inner-valence photoionization, it is unfortunate that there are insufficient experimental data with which to compare the present results.

The foregoing discussion of the convergence of the cross section ratios to the corresponding SIF ratios at high photon energy, per Figs. 7(b)–7(d) provides the foundation for assigning $6\ ^2\Sigma^+$, $9\ ^2\Sigma^+$, $13\ ^2\Sigma^+$, and $14\ ^2\Sigma^+$ as being of inner-valence origin, and this assignment permits us to discuss Figs. 7(a)–7(d) in terms of correlation. Since the breakdown of quasiparticle photoionization is attributed to near degeneracy of the single hole state with $2h$-$1p$ states, close contemplation of the $2h$-$1p$ states is important. If we are considering ionization from, for example, the 3σ orbital, then the $2h$-$1p$ configuration $3\sigma^{-1}1\pi^{-1}2\pi^1$ resembles a single $1\pi^{-1}2\pi^1$ excitation on top of the ionization and this is called a shake-up. Alternately, even if ionization occurs from the 3σ orbital there are $2h$-$1p$ configurations such as $5\sigma^{-1}1\pi^{-1}2\pi^1$ which may contribute to the indirect term and, at least in the case of interchannel coupling, Becker and Shirley referred to these as conjugate shake-ups. Distinguishing between the two in this manner can be confusing since the configuration $5\sigma^{-1}1\pi^{-1}2\pi^1$ can also be viewed as a shake-up of $5\sigma^{-1}$. Cederbaum *et al.*and Becker and Shirley classified both shake-up and conjugate shake-up states as arising from final-state configuration interaction. Inasmuch as there is no *a priori* reason why the nonorthogonality or indirect terms should vanish with increasing photon energy [condition (3) for Eq. (7) to be valid, *vida supra*] and the previous work on the inner valence photoionization of acetylene suggests that indirect terms, containing contributions from both of these types of $2h$-$1p$ states, can be significant to a photon energy of hundreds of eV, it may be confusing to refer to these contributions in terms of correlation because correlation is not typically associated with such high photon energies. We will refer to these terms as shake-up and conjugate shake-up contributions per Becker and Shirley. Another issue relating to correlation and pertinent to the present results is that, because the present calculations employ fully correlated targets and initial states, both the MCCI and SCCI scattering functions may inherently include both shake-up and conjugate shake-up type contributions, though only the MCCI scattering functions will *explicitly* have $2h$-$1p$ configurations from other channels. Thus, from the standpoint of the type of calculation we describe here, discussing these contributions in terms of correlation, can become ambiguous because there is more than one level of correlation built into the calculation.

In Becker and Shirley's description of energy-dependent correlation effects satellites which originate from shake-up contributions should display a satellite to main ratio which is very low at threshold and gradually increases to a constant value at high energies. Conversely, satellites which originate from conjugate shake-up contributions should display a satellite to main ratio which is high at threshold and gradually decreases to a constant value at high energies. The former

behavior is expected because orbital relaxation effects at energies well below the sudden limit result in decreased satellite intensity; the residual ion state orbitals have time to relax from potential excitations accompanying photoionization into a main hole state. Likewise, conjugate shake-up contributions, particularly in the form of interchannel coupling, are thought to be more important towards threshold, resulting in increased satellite intensity toward threshold. Looking at the most important CSF's for HCN in Table III, the conjugate shake-up configurations greatly predominate over shake-up configurations if we adhere to Cederbaum *et al.*'s terminology of a shake-up as being a single excitation on top of the main hole (in this case inner valence) photoionization. In HCN, of the four inner-valence satellites $6\ ^2\Sigma^+$, $9\ ^2\Sigma^+$, $13\ ^2\Sigma^+$, and $14\ ^2\Sigma^+$, the only inner-valence shake-up configuration in Table III is $3\sigma^{-1}1\pi^{-2}2\pi^2$, a doubly excited state which is a relatively minor CSF of $14\ ^2\Sigma^+$. Moreover, since the breakdown of molecular-orbital photoionization is thought to result from degeneracy between a main hole state and $2h$-$1p$ states, we may anticipate more conjugate shake-up terms that are degenerate with $3\sigma^{-1}$ than inner-valence shake-up terms, many of which will lie at too high an energy. Still, though the CSF's lead us to expect that essentially all of the HCN inner-valence satellites should display conjugate shake-up behavior, all of them display the shake-up energy dependence described by Becker and Shirley. We note that this discrepancy between the CSF's not appearing as shake-ups in the Cederbaum *et al.* terminology and leading to states which display shake-up behavior in the Becker and Shirley terminology appears to be a result of the embryonic state of the current knowledge of the dynamics of inner valence photoionization. A future direction in inner-valence photoionization work would be to separate the conjugate shake-up contributions from the shake-up contributions, and examine both as a functions of photon energy.

Above we noted that for HCN any choice of an inner-valence satellite can be used as the main line in Eq. (7), and, as long as the satellite used in the numerator is of the same provenance as the main line, the anticipated convergence behavior will be observed. Figures 8(a) and 8(b) illustrate how, according to the Becker-Shirley system, the $9\ ^2\Sigma^+$ state displays conjugate shake-up behavior when $13\ ^2\Sigma^+$ is used as the main line [Fig. 8(a)], but shake-up behavior in when $6\ ^2\Sigma^+$ is used as the main line [Fig. 8(b)]. Since the above arguments lead us to expect more conjugate shake-up states that are quasidegenerate with the inner-valence hole than shake-ups, another way of looking at Figs. 7(a)–7(d) is that $6\ ^2\Sigma^+$, $9\ ^2\Sigma^+$, $14\ ^2\Sigma^+$, and $13\ ^2\Sigma^+$ are all conjugate shake-up states, and that whenever the ''satellite to main'' cross-section ratio is plotted, the interchannel coupling terms of the state with lower photoelectron kinetic energy are large enough to strongly affect the cross-section ratio and hence determine the phenomenological behavior. However, in this scenario we expect the reverse of the trends illustrated in Fig. 8. If, alternately, we view the state with lower photoelectron kinetic energy as evincing stronger adiabaticity in the photoionization process, then whenever the satellite to main cross-section ratio is plotted such that the state in the numerator has a lower photoelectron kinetic energy, the numerator is smaller than the denominator because of the orbital relaxation effects near threshold and the shake-up phenomenological behavior results. Conversely, whenever the state in the denominator has a lower photoelectron kinetic energy, relaxation is more pronounced for the state in the denominator and the phenomenological ''conjugate shake-up'' behavior is observed. This explains why $9\ ^2\Sigma^+$ is a shake-up relative to $6\ ^2\Sigma^+$, and a conjugate shake-up relative to $13\ ^2\Sigma^+$, but is not the only explanation for the behavior. Becker and Shirley did not direct their work to situations wherein, as with the inner-valence study here, the main line is energetically above the satellite, and in their work the phenomenological behavior was based on the kinetic energy of the photoelectron rather than its binding energy. However, we find that the trends in Figs. 7 and 8 are unchanged when plotted in terms of the photoelectron kinetic energy. For inner-valence work, whenever a situation arises that the main line has a higher binding energy than the satellite to which it is compared, as for example in Fig. 8(a), the normal energy-dependent behavior for both shake-ups and conjugate shake-ups is reversed.

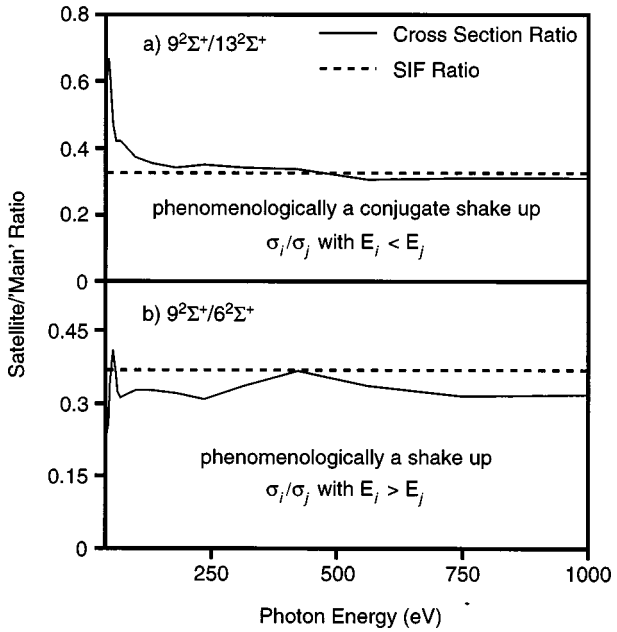

FIG. 8. Illustration of how the phenomenological behaviors of the satellite and main cross-section ratio depend on whether the satellite binding energy is higher or lower than that of the state chosen for the ''main line.'' (a) $9\ ^2\Sigma^+/13\ ^2\Sigma^+$. (b) $9\ ^2\Sigma^+/6\ ^2\Sigma^+$.

In the preceding paragraph, we provided an explanation for the behavior observed in Fig. 8 which is based on adiabaticity. A purely quantitative view of the Fig. 8 results from an examination of the photoionization cross sections in Figs. 2 and 3. If two functions behaving as exponentials and having exponentials that differ by at most a constant are ratioed, then the result will be a constant. In Figs. 2 and 3 we see that the photoionization cross sections behave as exponential functions at higher photon energy, and in Figs. 7 and 8 we see how the resulting ratios of any two cross sections are constant. However, in Figs. 2 and 3 we see that the cross sections generally flatten toward threshold and deviate from the exponential behavior that they exhibit at higher photon energies. It is this change in the energy-dependent near threshold behavior of the cross sections relative to each other that results in the nonconstant value of the ratios in Figs. 7

and 8 at lower photon energies. In our continuing studies on inner-valence photoionization, we are examining the causes of the cross-section energy dependence from low to high photon energy more closely.

IV. SUMMARY

Although there is little experimental data on the photoionization of HCN, the present theoretical results agree well with the one available PES spectrum of the HCN satellite region. Also, eigenphase sum results indicate that there is a σ shape resonance at $\sim$18–30 eV above threshold in the $1\ ^2\Sigma^+$ and $2\ ^2\Sigma^+$ channels which has not previously been characterized. With respect to the inner valence photoionization of HCN, this system provides an example of the complete breakdown of the quasiparticle picture of photoionization. In this study we find that the inner-valence hole is split into four states with significant intensity; these are $6\ ^2\Sigma^+$, $9\ ^2\Sigma^+$, $13\ ^2\Sigma^+$, and $14\ ^2\Sigma^+$. Also, there is one satellite state of mixed inner- and outer-valence provenance which appears as a shoulder on the high-binding-energy side of the $4\sigma^{-1}$ hole state. Cross-section ratios of any two inner-valence states converge at high photon energy to the corresponding SIF ratio, and, when the state has the higher photoelectron kinetic energy, consistently display the shake-up behavior described by Becker and Shirley. When the state in the numerator has the higher photoelectron kinetic energy, the cross-section ratio of any two inner valence states displays the conjugate shake-up behavior described by Becker and Shirley.

ACKNOWLEDGMENTS

We gratefully acknowledge support of this work by the Welch Foundation (Grant No. A-1020) and the support of the Texas A&M University Supercomputing Facility. M.C.W. thanks the U.S. Environmental Protection Agency for financial support.

[1] M. Wells and R. R. Lucchese, J. Chem. Phys. **110**, 6365 (1999).
[2] A. Omont, C. Loup, T. Forveille, P. T. Hekkert, H. Habing, and P. Sivagnanam, Astron. Astrophys. **267**, 515 (1993).
[3] S. T. Ridgway, D. N. B. Hall, S. G. Kleinmann, D. A. Weinburger, and R. S. Wojslaw, Nature (London) **264**, 345 (1976).
[4] E. Nercessian, S. Guilloteau, A. Omont, and J. J. Benayoun, Astron. Astrophys. **210**, 225 (1989).
[5] N. Shafizadeh, J.-H. Fillion, D. Gauyacq, and S. Couris, Philos. Trans. R. Soc. London, Ser. A **355**, 1637 (1997).
[6] J. Wirsich, Astrophys. J. **424**, 370 (1994).
[7] L. Nahon, P. Morin, M. Larzilliere, and I. Nenner, J. Chem. Phys. **96**, 3628 (1992).
[8] H. Köppel, L. S. Cederbaum, W. Domcke, and W. v. Niessen, Chem. Phys. **37**, 303 (1979).
[9] A. J. Lorquet, J. C. Lorquet, J. Delwiche, and M. J. Hubin-Franskin, J. Chem. Phys. **76**, 4692 (1982).
[10] J. C. Lorquet and V. B. Pavlov-Verevkin, J. Chem. Phys. **93**, 520 (1990).
[11] J. P. Hansoul, C. Galloy, and J. C. Lorquet, J. Chem. Phys. **68**, 4105 (1978).
[12] R. T. Wiedmann and M. G. White, J. Chem. Phys. **102**, 5141 (1995).
[13] C. Fridh and L. Åsbrink, J. Electron Spectrosc. Relat. Phenom. **7**, 119 (1975).
[14] J. H. D. Eland, T. Field, P. Baltzer, and D. M. Hirst, Chem. Phys. **229**, 149 (1998).
[15] V. H. Dibeler and S. K. Liston, J. Chem. Phys. **48**, 4765 (1968).
[16] J. Berkowitz, W. A. Chupka, and T. A. Walter, J. Chem. Phys. **50**, 1497 (1969).
[17] J. M. Hollas and T. A. Sutherley, Mol. Phys. **24**, 1123 (1972).
[18] J. A. Nuth and S. Glicker, J. Quant. Spectrosc. Radiat. Transf. **28**, 223 (1982).
[19] D. W. Turner, C. Baker, A. D. Baker, and C. R. Brundle, *Molecular Photoelectron Spectroscopy* (Wiley-Interscience, London, 1970).
[20] J. Wirsich, Spectrosc. Lett. **23**, 741 (1990).
[21] J. Kreile, A. Schweig, and W. Thiel, Chem. Phys. Lett. **87**, 473 (1982).
[22] D. C. Frost, S. T. Lee, and C. A. McDowell, Chem. Phys. Lett. **23**, 472 (1973).
[23] L. Åsbrink, C. Fridh, and E. Lindholm, Chem. Phys. **27**, 159 (1978).
[24] L. S. Cederbaum, W. Domcke, J. Schirmer, and W. v. Niessen, Adv. Chem. Phys. **65**, 115 (1986).
[25] L. S. Cederbaum, J. Schirmer, W. Domcke, and W. v. Niessen, Int. J. Quantum Chem. **XIV**, 593 (1978).
[26] L. S. Cederbaum, W. Domcke, J. Schirmer, W. v. Niessen, G. H. F. Diercksen, and W. P. Kraemer, J. Chem. Phys. **69**, 1591 (1978).
[27] U. Becker and D. A. Shirley, Phys. Scr. **T31**, 56 (1990).
[28] R. E. Stratmann, R. W. Zurales, and R. R. Lucchese, J. Chem. Phys. **104**, 8989 (1996).
[29] R. E. Stratmann, G. Bandarage, and R. R. Lucchese, Phys. Rev. A **51**, 3756 (1995).
[30] R. E. Stratmann and R. R. Lucchese, J. Chem. Phys. **102**, 8493 (1995).
[31] P. J. Knowles and H.-J. Werner, Chem. Phys. Lett. **115**, 259 (1985).
[32] H.-J. Werner, Adv. Chem. Phys. **LXIX**, 1 (1987).
[33] H.-J. Werner and P. J. Knowles, *MOLPRO* (University of Birmingham, Birmingham, 1996).
[34] G. Winnewisser, A. G. Maki, and D. R. Johnson, J. Mol. Spectrosc. **39**, 149 (1971).
[35] R. R. Lucchese and R. W. Zurales, Phys. Rev. A **44**, 291 (1991).
[36] R. C. Morrison and G. H. Liu, J. Comput. Chem. **13**, 1004 (1992).
[37] D. Heryadi, D. L. Yeager, J. T. Golab, and J. A. Nichols, Theor. Chim. Acta **90**, 273 (1995).
[38] R. W. Zurales, E. Stratmann, S. Botting, and R. R. Lucchese, in *Photon and Electron Collisions with Atoms and Molecules*, edited by P. G. Burke and C. J. Joachain (Plenum, New York, 1997).
[39] M. C. Wells, Ph.D. thesis, Texas A&M University, 1999.
[40] R. R. Lucchese, J. Chem. Phys. **92**, 4203 (1990).

[41] G. Bandarage and R. R. Lucchese, Phys. Rev. A **47**, 1989 (1993).
[42] R. R. Lucchese, G. Raseev, and V. McKoy, Phys. Rev. A **25**, 2572 (1982).
[43] A. M. Bradshaw, W. Eberhardt, H. J. Levinson, W. Domcke, and L. S. Cederbaum, Chem. Phys. Lett. **70**, 36 (1980).
[44] J. J. Yeh and I. Lindau, At. Data Nucl. Data Tables **32**, 1 (1985).
[45] R. Das, C. Wu, A. G. Mihill, E. D. Poliakoff, K. Wang, and V. McKoy, J. Phys. Chem. **99**, 1741 (1995).
[46] J. A. Stephens and D. Dill, Phys. Rev. A **31**, 1968 (1985).
[47] B. Basden and R. R. Lucchese, Phys. Rev. A **37**, 89 (1988).
[48] E. D. Poliakoff, S. Kakar, and R. A. Rosenberg, J. Chem. Phys. **96**, 2740 (1992).
[49] M. S. Moghaddam, S. J. Dejardins, A. D. O. Bawagan, K. H. Tan, Y. Wang, and E. R. Davidson, J. Chem. Phys. **103**, 10 537 (1995).